photonics

MDPI

Article

Integrated Mobile Visible Light Communication and Positioning Systems Based on Decision Feedback Channel Estimation

Ruoxuan Wang [1], Yuzhe Sun [1], Zhongxu Liu [2], Mingyi Gao [1] and Xiaodi You [1,*]

[1] School of Electronic and Information Engineering, Soochow University, Suzhou 215000, China; 2128410028@stu.suda.edu.cn (R.W.); 20215228065@stu.suda.edu.cn (Y.S.); mygao@suda.edu.cn (M.G.)
[2] Department of Electrical and Electronic Engineering, The Hong Kong Polytechnic University, Hong Kong; zhongxu.liu@connect.polyu.hk
* Correspondence: xdyou@suda.edu.cn

Abstract: Visible light communication (VLC) and visible light positioning (VLP) systems are usually designed separately to prevent mutual interference, while terminal mobility often introduces challenges that can degrade their performance. In this paper, we propose an integrated visible light communication and positioning (VLCP) scheme designed for mobile scenarios, encompassing both multiple-input–single-output (MISO) and multiple-input–multiple-output (MIMO) configurations. This scheme integrates both functionalities into a unified system. Utilizing decision feedback channel estimation (DFCE), we effectively estimate the dynamic channel state information (CSI) for both VLC and VLP, thereby potentially enhancing both communication and positioning performance. Simulation results across various routes verify the effectiveness of the proposed scheme. It is observed that when the terminal moves at 1 m/s, the VLCP scheme with DFCE can maintain reliable transmission quality, ensuring bit error rates (BERs) consistently below 1.3×10^{-2}. Additionally, the mean positioning errors remain within the centimeter range in different routes, not exceeding 4.3 cm and 15.5 cm in the MISO and MIMO scenarios, respectively.

Keywords: visible light communication and positioning (VLCP); decision feedback channel estimation (DFCE); multiple-input–single-output (MISO); multiple-input–multiple-output (MIMO)

Citation: Wang, R.; Sun, Y.; Liu, Z.; Gao, M.; You, X. Integrated Mobile Visible Light Communication and Positioning Systems Based on Decision Feedback Channel Estimation. *Photonics* **2024**, *11*, 537. https://doi.org/10.3390/photonics11060537

Received: 30 April 2024
Revised: 28 May 2024
Accepted: 29 May 2024
Published: 4 June 2024

1. Introduction

With the development of mobile Internet and industrial Internet of Things, there has been a growing demand for high-efficiency indoor data access and high-accuracy positioning. Indoor visible light communication (VLC) based on light-emitting diodes (LEDs) has emerged as a promising solution, leveraging the advantages of visible light for lighting, communication, and positioning purposes [1–3], providing an additional communication channel in indoor environments where radio frequency (RF) communication may face challenges like data insecurity, interference, and limited spectrum availability. Specifically, VLC can be applied to indoor positioning, often referred to as visible light positioning (VLP) [4], offering benefits such as high accuracy, low cost, and immunity to electromagnetic interference [5,6].

However, conventional VLC and VLP systems are typically designed and deployed independently. When deployed within the same indoor environment to provide both communication and positioning services simultaneously and share similar bandwidth resources, these systems may struggle to deliver high-quality performance in their respective functions due to frequency interference. Thus, integrated visible light communication and positioning (VLCP) systems using multiplexing techniques like time division multiplexing (TDM), frequency division multiplexing (FDM), and code division multiplexing (CDM) can address this issue. TDM, the simplest method, segregates VLC and VLP signals into different time slots [7,8]. With FDM, VLC and VLP signals occupy distinct frequency subcarriers for simultaneous transmission and positioning [9–13]. CDM assigns unique

spreading codes to VLC and VLP signals, which are then differentiated through despreading codes [8,14,15]. However, commercial LEDs typically offer a narrow bandwidth, often just a few megahertz. Consequently, in scenarios where both communication and positioning are equally vital, effectively managing limited bandwidth resources to ensure reliable communication and accurate positioning poses a significant challenge for integrated VLCP design. The mentioned schemes may fail to allocate sufficient communication resources for both VLC and VLP simultaneously. To optimize the utilization of constrained bandwidth resources, researchers have proposed realizing VLP based on the channel state information (CSI) during VLC [16–18]. In [16], the estimated frequency domain transfer function (FDTF) of VLC channels was utilized for ranging, enabling VLP. In [17], the distances between LEDs and the PD were estimated through the received signal strength (RSS) of VLC channels, followed by trilateration to achieve VLP. However, the above studies focus on the scenario where the terminal was stationary and do not consider the case of terminal movement.

From the user's perspective, terminal mobility poses a significant and challenging issue in mobile VLCP systems. On one hand, in mobile VLC, terminal mobility causes fluctuations in the optical channel, impacting the VLC performance [19]. Various strategies have been proposed to enhance the link performance. In [20], a decision feedback channel estimation (DFCE) scheme was proposed to estimate the time-varying CSI in mobile VLC systems. In [21,22], space–time block coding (STBC) was employed to enhance the robustness of mobile VLC against time-varying CSI. However, these studies mainly focus on single-input–single-output (SISO) or multiple-input–single-output (MISO) systems, overlooking the potential of multiple-input–multiple-output (MIMO) systems, which have been demonstrated to boost the capacity and reliability of VLC systems [23,24]. On the other hand, in mobile VLP, the optical channel fluctuation also affects the positioning performance. While studies have targeted mobile VLP, they often involve fixing terminals at discrete locations to receive VLP signals [25,26]. Few studies have considered the continuous movement of terminals. For a mobile receiver, when conducting VLP discretely (e.g., using the RSS scheme), the positioning accuracy along the moving trajectory will inevitably deteriorate due to channel variations. To enhance accuracy, reducing the time interval of positioning is necessary. However, this entails transmitting more VLP signals, leading to reduced spectrum efficiency. Some studies address this by utilizing CSI as a feature fingerprint and analyzing it through machine learning [27–29]. Nevertheless, this approach demands significant data processing and computational power from mobile terminals. It also requires extensive data collection for model training, and any environmental changes necessitate repeating the training steps, which hampers system portability. Hence, new approaches are needed to enhance mobile VLP. In summary, current research on mobile VLC and VLP has limitations, with studies on integrated mobile VLCP still being relatively scarce.

In this paper, we propose an integrated mobile VLCP scheme designed for both MISO and MIMO scenarios, leveraging DFCE to efficiently estimate dynamic CSI for both VLC and VLP. The scheme begins with using training symbols to acquire initial CSI at discrete locations. Subsequently, it transitions to a decision feedback mode to continuously track and estimate subsequent CSI as the receiver moves. For the MISO scenario, specific groups of LEDs are selected from multiple LEDs to transmit identical VLC signals simultaneously, ensuring sufficient signal-to-noise ratios (SNRs). These groups of LEDs vary in each time slot within a cycle, allowing for the extraction of CSI related to VLC from multipath channels. This information is then used, via DFCE, to determine the range between each LED and the PD for VLP purposes. For the MIMO scenario, we utilize STBC to enhance the bit error rate (BER) performance. The improved transmission quality contributes to more accurate VLC-based CSI via DFCE, thereby further enhancing positioning accuracy. Our extensive simulations evaluate both communication and positioning performance as the receiver moves through different routes within a 5 m $\times$ 5 m $\times$ 3 m indoor space. We analyze the effects of LED transmit power and receiver velocities on communication performance. For positioning accuracy, we investigate the impacts of observation block

length, receiver velocities, and other relevant factors. The results indicate that in both MISO and MIMO scenarios, implementing DFCE maintains the BERs between approximately 10^{-4} and 10^{-2} for mobile VLC, while successfully achieving centimeter-level mobile VLP. Note that part of this work was previously presented in our short conference paper [30], which only focused on the MIMO scenario. However, in this expanded study, we conduct a comprehensive investigation covering both MISO and MIMO scenarios, as well as addressing additional issues.

The rest of the paper is organized as follows: Section 2 introduces the principle of the proposed integrated mobile VLCP scheme, considering both MISO and MIMO scenarios. Simulation results and discussions are presented in Section 3. Finally, we conclude the paper in Section 4.

2. Proposed Integrated Mobile VLCP Scheme

Figure 1 illustrates the schematic diagram of an integrated mobile VLCP system model, considering both MISO and MIMO configurations. The system comprises N_T LEDs serving as transmitting antennas installed in the ceiling to transmit VLC signals. The coordinate of the ith LED (i = 1, 2, …, N_T) is known and denoted as (x_i, y_i, z_i). In this work, we focus on the scenario where N_T = 4. The mobile receiver is equipped with N_R PDs serving as receiving antennas, positioned in the receiving plane. For the MISO scenario, N_R = 1, whereas for MIMO, N_R = 2 is assumed. Each PD is upward-oriented to receive VLC signals. The three-dimensional (3D) coordinate of the jth PD (j = 1, 2, …, N_R) is (x_{rj}, y_{rj}, z_{rj}), with its two-dimensional (2D) horizontal coordinate (x_{rj}, y_{rj}) being unknown, and its vertical coordinate (z_{rj}) known. At the receiver, channel estimation is conducted to recover the VLC signal. The acquired CSI is then utilized for receiver localization, enabling simultaneous VLC and VLP within the same system.

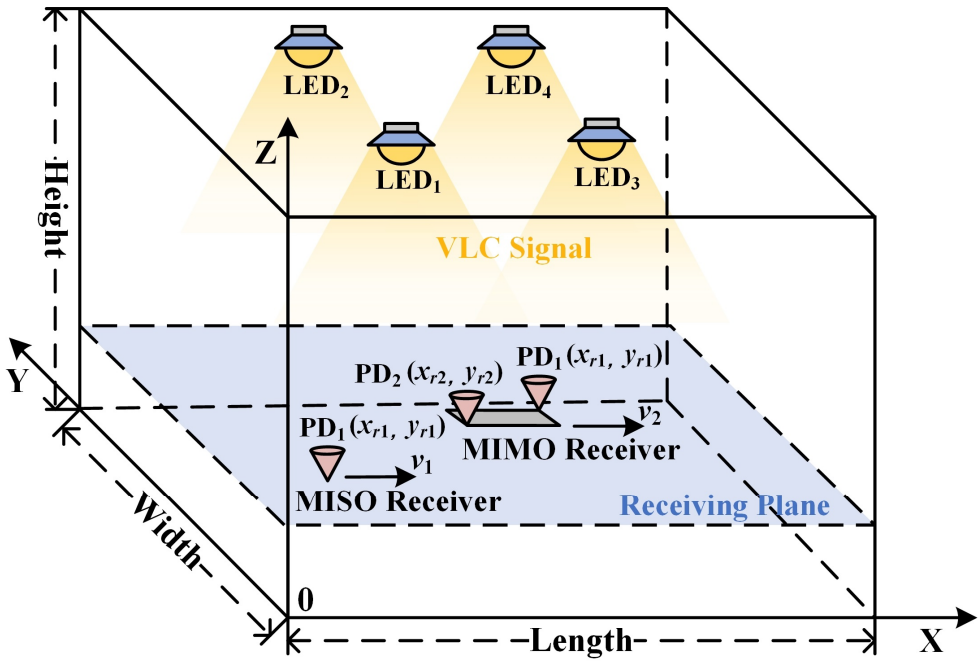

Figure 1. Schematic diagram of an integrated mobile VLCP system model.

2.1. Proposed Scheme for MISO Configuration

We first consider the MISO scenario. Figure 2 depicts the block diagram of the proposed integrated mobile VLCP scheme for MISO. At the transmitter, serial source bits are converted into quadrature amplitude modulation (QAM) symbols $X(k)$, where k represents the subcarrier channel index (k = 1, 2, 3, …). These QAM symbols are then modulated into the DC-biased optical OFDM (DCO-OFDM) signal $x(t)$. Next, $x(t)$ enters

the LED selection stage, where the selector determines the groups of LEDs transmitting the identical $x(t)$ simultaneously. In our VLCP system, the total number of LEDs is four, which is commonly used to provide adequate and uniform light distribution in the receiving plane. From a communication perspective, adopting more LEDs can enhance SNRs for better link performance. Based on this, a simple way is to adopt all LEDs to send the same signal. However, from a positioning perspective, to enable trilateration, at least three LEDs are required, and the distances between each LED and the PD need to be estimated separately. Using a single-LED setup is inadequate to support trilateration as it does not provide enough distance measurements. For our four-LED setup, using all four LEDs to transmit signals simultaneously does not allow for the establishment of sufficient equations to calculate the distances between LEDs and the PD. To optimize both communication and positioning, different groups of LEDs can be used to transmit signals and calculate the CSI from multipath channels for VLP. For each group, a subset of N_{used} LEDs out of four LEDs is selected to transmit the same signal. In the case where $N_{used} = 1$, each of the four LEDs transmits the signal in one slot, but this configuration may not optimize the SNR, leading to reduced DFCE accuracy. The same issue arises for $N_{used} = 2$. Since involving more LEDs can enhance the SNR, we focus on $N_{used} = 3$, dividing the four LEDs into four groups: Group 1 (LED1, LED2, LED3), Group 2 (LED1, LED2, LED4), Group 3 (LED1, LED3, LED4), and Group 4 (LED2, LED3, LED4). This division is the optimized solution that ensures both signal recovery and optimized link performance at the receiver. The number of groups equals the total slots per cycle. After each cycle, the CSI can be estimated for VLCP and fed back for the next cycle. The four slots form a VLCP data block, and for the nth VLCP data block, the LED selection is determined by the LED selection matrix:

$$\mathbf{X}^n(t) = \begin{bmatrix} x_1^{n,1}(t) & x_2^{n,1}(t) & x_3^{n,1}(t) & 0 \\ x_1^{n,2}(t) & x_2^{n,2}(t) & 0 & x_4^{n,2}(t) \\ x_1^{n,3}(t) & 0 & x_3^{n,3}(t) & x_4^{n,3}(t) \\ 0 & x_2^{n,4}(t) & x_3^{n,4}(t) & x_4^{n,4}(t) \end{bmatrix}. \tag{1}$$

Here, $x_i^{n,w}(t)$ represents the wth OFDM symbol emitted by the ith LED in the nth VLCP data block, where $i = 1, 2, 3, 4$ and $w = 1, 2, 3, 4$. With the same w, $x_i^{n,w}(t)$ in each row of the matrix represents the same signals transmitted during the same slot, and different i values represent different expressions of the same signals emitted by different LEDs. After passing through multipath channels, the VLC signal arrives at the mobile receiver equipped with a single PD, denoted as PD1. Following light-to-current inversion, DC filtering, and time-to-frequency transformation, the electrical signal of the nth VLCP data block received by PD1 in the frequency domain can be expressed as follows:

$$\mathbf{Y}^n(k) = \mathbf{X}^n(k)\mathbf{H}^n(k) + \mathbf{N}^n(k). \tag{2}$$

Here, $\mathbf{X}^n(k)$ is the frequency representation of $\mathbf{x}^n(t)$, implying that each element $X_i^{n,l}(k)$ ($l = 1, 2, 3, 4$) in $\mathbf{X}^n(k)$ is the frequency representation of $x_i^{n,w}(t)$ in $\mathbf{x}^n(t)$ after Fourier transform. Thus, for the nth VLCP data block, $X_i^{n,l}(k)$ is the kth transmitted subcarrier symbol of the lth OFDM symbol at the ith LED, $\mathbf{Y}^n(k) = [Y^{n,1}(k), Y^{n,2}(k), Y^{n,3}(k), Y^{n,4}(k)]^{\mathrm{T}}$, where $Y^{n,l}(k)$ is the kth received subcarrier symbol of the lth OFDM symbol at PD1, $\mathbf{H}^n(k) = [H_1^n(k), H_2^n(k), H_3^n(k), H_4^n(k)]^{\mathrm{T}}$, where $H_i^n(k)$ is the FDTF of the channel between the ith LED and PD1, and $\mathbf{N}^n(k)$ is the noise matrix. Next, to recover the transmitted signal, we equalize the multipath channel. After zero-forcing equalization, the kth OFDM subcarrier symbol in the nth VLCP data block can be expressed as follows:

$$\hat{\mathbf{S}}^n(k) = \left[\frac{Y^{n,1}(k)}{\hat{H}_{T1\_total}^n(k)}, \frac{Y^{n,2}(k)}{\hat{H}_{T2\_total}^n(k)}, \frac{Y^{n,3}(k)}{\hat{H}_{T3\_total}^n(k)}, \frac{Y^{n,4}(k)}{\hat{H}_{T4\_total}^n(k)} \right]^T, \tag{3}$$

where $\hat{H}^n_{Tw\_total}(k)$ (w = 1, 2, 3, 4) is the estimated FDTF of the channel between all LEDs activated in the wth time slot and PD1.

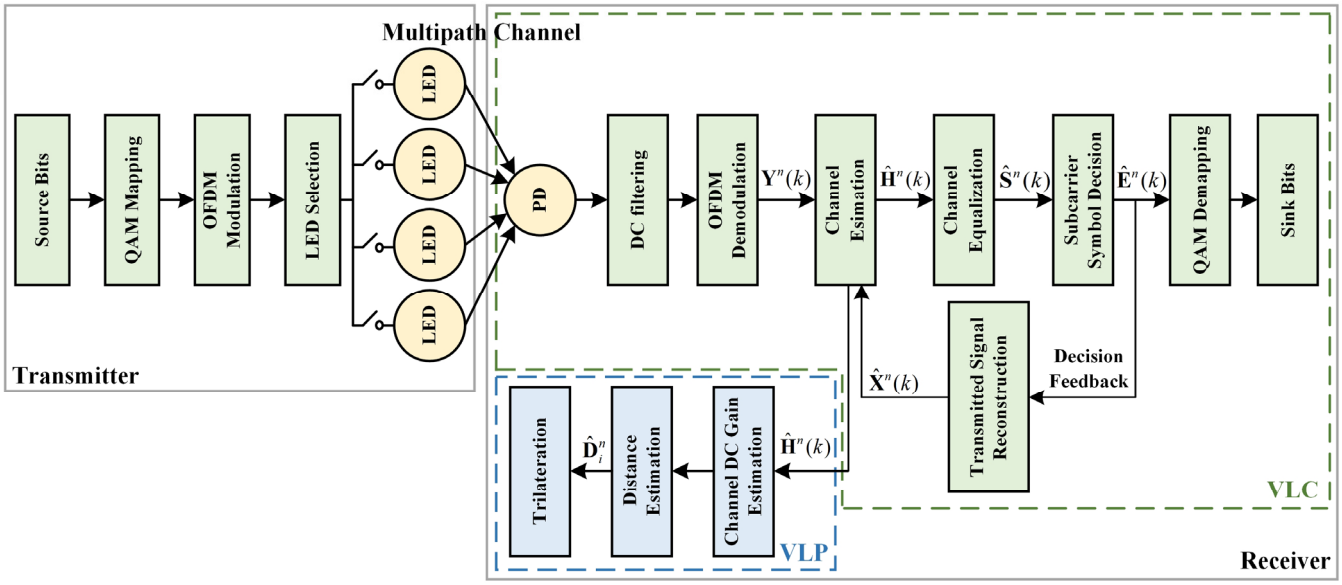

Figure 2. Block diagram of the integrated mobile VLCP scheme for MISO configuration.

According to Equation (3), before channel estimation, the receiver needs to have a priori knowledge of the CSI. Conventionally, training symbols at the beginning of each OFDM packet are employed for CSI estimation, assuming that the channel remains constant throughout the entire packet. However, in a mobile VLCP terminal, the channel characteristics vary over time. Consequently, the CSI estimated from training symbols may differ from that experienced by subsequent data symbols, leading to errors in CSI estimation and potentially affecting system performance. To effectively track the dynamic channel and achieve more accurate CSI, we implement the DFCE scheme in our system [20]. This scheme initially employs training symbols at the beginning of each OFDM packet to estimate the initial CSI. Subsequently, the estimated CSI is utilized to calculate $\hat{\mathbf{S}}^n(k)$ using Equation (3). Based on $\hat{\mathbf{S}}^n(k)$, the receiver can derive the decision value $\hat{\mathbf{E}}^n(k)$ to recover the original transmitted signal. The feedback of $\hat{\mathbf{E}}^n(k)$ is utilized to reconstruct the estimated transmitted signal matrix $\hat{\mathbf{X}}^n(k)$. Finally, $\hat{\mathbf{X}}^n(k)$ and $\mathbf{Y}^n(k)$ are used to update the CSI for subsequent channel estimation in the next VLCP data block, given by the following:

$$\hat{\mathbf{H}}^{n+1}(k) = \frac{1}{L}\sum_{p=n-L+1}^{n} \mathbf{Y}^p(k)[\hat{\mathbf{X}}^p(k)]^{-1}, \tag{4}$$

where L is the observation block length for VLCP data blocks. Equation (4) averages out noise by incorporating multiple blocks. This process is repeated to recover subsequent VLCP data blocks until the end of each OFDM packet. By doing so, we effectively track and mitigate channel variations between neighboring VLCP data blocks, thereby enhancing the channel estimation accuracy. It is worth mentioning that, based on the LED selection matrix in Equation (1), $\hat{\mathbf{X}}^n(k)$ is always invertible, ensuring the implementation of Equation (4).

Meanwhile, benefiting from the enhanced channel estimation accuracy, the CSI, specifically $\hat{H}^n_{Tw\_total}(k)$, can further be utilized to estimate the location of the mobile receiver. Based on Equation (3) and the LED selection in Equation (1), the specific expansion of the FDTFs for the multipath channels can be derived as follows:

$$\begin{cases} \hat{H}^n_{T1\_total}(k) = \hat{H}^n_{DC,1}(0)e^{-j2\pi k\Delta f t_1} + \hat{H}^n_{DC,2}(0)e^{-j2\pi k\Delta f t_2} + \hat{H}^n_{DC,3}(0)e^{-j2\pi k\Delta f t_3} \\ \hat{H}^n_{T2\_total}(k) = \hat{H}^n_{DC,1}(0)e^{-j2\pi k\Delta f t_1} + \hat{H}^n_{DC,2}(0)e^{-j2\pi k\Delta f t_2} + \hat{H}^n_{DC,4}(0)e^{-j2\pi k\Delta f t_4} \\ \hat{H}^n_{T3\_total}(k) = \hat{H}^n_{DC,1}(0)e^{-j2\pi k\Delta f t_1} + \hat{H}^n_{DC,3}(0)e^{-j2\pi k\Delta f t_3} + \hat{H}^n_{DC,4}(0)e^{-j2\pi k\Delta f t_4} \\ \hat{H}^n_{T4\_total}(k) = \hat{H}^n_{DC,2}(0)e^{-j2\pi k\Delta f t_2} + \hat{H}^n_{DC,3}(0)e^{-j2\pi k\Delta f t_3} + \hat{H}^n_{DC,4}(0)e^{-j2\pi k\Delta f t_4} \end{cases}. \quad (5)$$

Here, $\hat{H}^n_{DC,i}(0)$ is the estimated channel DC gain between the ith LED and PD1, Δf is the subcarrier frequency interval, and t_i is the propagation time of the signal from the ith LED to PD1. By squaring both sides simultaneously and setting k = 1, we can obtain the estimated channel DC gain from each LED to PD1:

$$\begin{cases} \hat{H}^n_{DC,1}(0) \approx \frac{1}{3}[\left|\hat{H}^n_{T1\_total}(1)\right| + \left|\hat{H}^n_{T2\_total}(1)\right| + \left|\hat{H}^n_{T3\_total}(1)\right| - 2\left|\hat{H}^n_{T4\_total}(1)\right|] \\ \hat{H}^n_{DC,2}(0) \approx \frac{1}{3}[\left|\hat{H}^n_{T1\_total}(1)\right| + \left|\hat{H}^n_{T2\_total}(1)\right| + \left|\hat{H}^n_{T4\_total}(1)\right| - 2\left|\hat{H}^n_{T3\_total}(1)\right|] \\ \hat{H}^n_{DC,3}(0) \approx \frac{1}{3}[\left|\hat{H}^n_{T1\_total}(1)\right| + \left|\hat{H}^n_{T3\_total}(1)\right| + \left|\hat{H}^n_{T4\_total}(1)\right| - 2\left|\hat{H}^n_{T2\_total}(1)\right|] \\ \hat{H}^n_{DC,4}(0) \approx \frac{1}{3}[\left|\hat{H}^n_{T2\_total}(1)\right| + \left|\hat{H}^n_{T3\_total}(1)\right| + \left|\hat{H}^n_{T4\_total}(1)\right| - 2\left|\hat{H}^n_{T1\_total}(1)\right|] \end{cases}. \quad (6)$$

In our VLCP scheme, without loss of generality, we consider a VLC channel model where LEDs are assumed to follow a Lambertian radiation pattern [31]. Whether phosphor LEDs or RGB LEDs, as long as they follow this radiation pattern, they can be used in our system. Furthermore, for other types of radiation patterns, as long as the radiation pattern is known and the distances between LEDs and PDs can be determined from the estimated channel DC gains, these types of LEDs can also be used. Considering the Lambertian radiation model, the distance between the ith LED and PD1 can be estimated using the RSS scheme:

$$\hat{D}^n_i = \sqrt[m+3]{\frac{(m+1)AT_s(\varphi)g(\varphi)h^{m+1}}{2\pi\hat{H}^n_{DC,i}(0)}}, \quad (7)$$

where m is the Lambertian emission order, A is the effective area of the PD, $T_s(\varphi)$ is the optical filter gain, $g(\varphi)$ is the concentrator gain, and h is the vertical distance between the LEDs and the receiving plane.

Based on Equation (7), we can select three from the four estimated distances to estimate the location of the receiver. For example, using $\hat{D}^n_1$, $\hat{D}^n_2$, and $\hat{D}^n_3$, the horizontal coordinate of PD1 $(\hat{x}_{r1}, \hat{y}_{r1})$ can be estimated with trilateration by solving the following:

$$\begin{cases} \left(\hat{D}^n_1\right)^2 = (\hat{x}_{r1} - x_1)^2 + (\hat{y}_{r1} - y_1)^2 + h^2 \\ \left(\hat{D}^n_2\right)^2 = (\hat{x}_{r1} - x_2)^2 + (\hat{y}_{r1} - y_2)^2 + h^2 \\ \left(\hat{D}^n_3\right)^2 = (\hat{x}_{r1} - x_3)^2 + (\hat{y}_{r1} - y_3)^2 + h^2 \end{cases}. \quad (8)$$

In the MISO scenario, $(\hat{x}_{r1}, \hat{y}_{r1})$ can simply be assumed as the receiver's horizontal coordinate $(\hat{x}_R, \hat{y}_R)$. To enhance positioning accuracy, we can select different groups of $\hat{D}^n_i$ to obtain multiple solutions, i.e., $(\hat{x}^q_{r1}, \hat{y}^q_{r1})$ (q = 1, 2, 3, 4), and then take their average value $((\hat{x}^1_{r1} + \hat{x}^2_{r1} + \hat{x}^3_{r1} + \hat{x}^4_{r1})/4, (\hat{y}^1_{r1} + \hat{y}^2_{r1} + \hat{y}^3_{r1} + \hat{y}^4_{r1})/4)$ as the final estimated horizontal coordinate of the receiver.

It is worth noting that Equation (4) assumes equal weight coefficients for the VLCP data blocks within the observation block. When the receiver is static, maintaining the same weight coefficient does not affect CSI accuracy. However, for a mobile receiver, where the channel varies over time, the estimated channel from different VLCP data blocks varies as well. Specifically, the closer the VLCP data blocks, the greater their impact on the channel estimation of the current block. Therefore, optimizing the weight coefficients can lead to better performance. Generally, closer blocks are assigned higher weights, with the neighboring block potentially having the highest weight. By considering the unequal

weight coefficients, the CSI used for subsequent channel estimation in the next VLCP data block can be optimized as follows:

$$\hat{\mathbf{H}}^{n+1}(k) = \sum_{p=n-L+1}^{n} \frac{\alpha^{n-p}(1-\alpha)}{1-\alpha^{L}} \mathbf{Y}^{p}(k)[\hat{\mathbf{X}}^{p}(k)]^{-1}, \tag{9}$$

where α represents a forgotten factor ($0 < \alpha < 1$).

2.2. Proposed Scheme for MIMO Configuration

Next, we consider the MIMO scenario. Figure 3 illustrates the block diagram of the proposed indoor integrated mobile VLCP scheme for MIMO. At the transmitter, serial source bits are converted into multiple parallel data streams, mapped into QAM symbols, and encoded by STBC. Here, STBC is introduced to ensure the feasibility of DFCE in the MIMO scenario, with the encoding matrix depending on the number of transmitting antennas N_T. In this work, we focus on a 4×2 MIMO system, where the receiver has two PDs (PD1 and PD2). Thus, similar to the MISO case, in this MIMO configuration, there are also four slots in a VLCP data block. For the nth VLCP data block, the STBC encoding matrix is expressed as [32]:

$$\mathbf{X}^{n}(k) = \begin{bmatrix} X_1^{n,1}(k) & X_2^{n,2}(k) & X_3^{n,3}(k) & 0 \\ -X_1^{n,2*}(k) & X_2^{n,1*}(k) & 0 & X_4^{n,3}(k) \\ X_1^{n,3*}(k) & 0 & -X_3^{n,1*}(k) & X_4^{n,2}(k) \\ 0 & X_2^{n,3*}(k) & -X_3^{n,2*}(k) & -X_4^{n,1}(k) \end{bmatrix}, \tag{10}$$

where * is the conjugate operation and $X_i^{n,l}(k)$ (i = 1, 2, 3, 4 and l = 1, 2, 3, 4) is the kth transmitted subcarrier symbol of the lth OFDM symbol at the ith LED. Each row of the matrix corresponds to signals transmitted during the same slot. These STBC symbols are modulated into DCO-OFDM symbols and transmitted by each LED. Upon traversing the MIMO channel, the VLC signal arrives at the mobile receiver. Following light-to-current inversion, DC filtering, and OFDM demodulation, the signal received at the jth (j = 1, 2) PD in the nth STBC block is represented in the frequency domain as follows:

$$\mathbf{Y}_j^{n}(k) = \mathbf{X}^{n}(k)\mathbf{H}_j^{n}(k) + \mathbf{N}_j^{n}(k). \tag{11}$$

Here, $\mathbf{Y}_j^{n}(t) = [Y_j^{n,1}(k), Y_j^{n,2}(k), Y_j^{n,3}(k), Y_j^{n,4}(k)]^{\mathrm{T}}$, where $Y_j^{n,l}(k)$ is the kth received subcarrier symbol of the lth OFDM symbol at the jth PD, $\mathbf{H}_j^{n}(k) = [H_{j1}^{n}(k), H_{j2}^{n}(k), H_{j3}^{n}(k), H_{j4}^{n}(k)]^{\mathrm{T}}$, where $H_{ji}^{n}(k)$ is the FDTF of the channel between the ith LED and the jth PD, and $\mathbf{N}_j^{n}(k)$ is the noise matrix. The parallel OFDM data are then decoded by STBC, demapped, and finally converted into serial sink bits. Following STBC decoding, the kth OFDM subcarrier symbol in the nth STBC matrix is decoded by [32]:

$$\hat{\mathbf{S}}^{n}(k) = \frac{\begin{bmatrix} \hat{H}_{j1}^{n*}(k)Y_j^{n,1}(k) + \hat{H}_{j2}^{n}(k)Y_j^{n,2*}(k) - \hat{H}_{j3}^{n*}(k)Y_j^{n,3*}(k) - \hat{H}_{j4}^{n*}(k)Y_j^{n,4}(k) \\ \hat{H}_{j2}^{n*}(k)Y_j^{n,1}(k) - \hat{H}_{j1}^{n}(k)Y_j^{n,2*}(k) + \hat{H}_{j4}^{n*}(k)Y_j^{n,3}(k) - \hat{H}_{j3}^{n}(k)Y_j^{n,4*}(k) \\ \hat{H}_{j3}^{n*}(k)Y_j^{n,1}(k) + \hat{H}_{j4}^{n}(k)Y_j^{n,2}(k) + \hat{H}_{j1}^{n}(k)Y_j^{n,3*}(k) + \hat{H}_{j2}^{n}(k)Y_j^{n,4*}(k) \end{bmatrix}}{\sum_{i=1}^{4}\left|\hat{H}_{ji}^{n}(k)\right|^{2}}. \tag{12}$$

Based on Equation (12), prior to STBC decoding, the receiver requires a priori knowledge of CSI. To track time-varying channels, we employ DFCE to obtain the CSI, similar to the MISO scenario. The training sequence is used to acquire the initial CSI, resulting in $\hat{\mathbf{S}}^{n}(k)$. Then, based on $\hat{\mathbf{S}}^{n}(k)$, the receiver derives the decision value $\hat{\mathbf{E}}^{n}(k)$, which is encoded by STBC to reconstruct the estimated transmitted signal matrix $\hat{\mathbf{X}}^{n}(k)$. Finally, $\hat{\mathbf{H}}_j^{n+1}(k)$ is

updated for subsequent calculations of $\hat{\mathbf{S}}^{n+1}(k)$. With equal weight coefficients, $\hat{\mathbf{H}}_j^{n+1}(k)$ can be expressed as follows:

$$\hat{\mathbf{H}}_j^{n+1}(k) = \frac{1}{L}\sum_{p=n-L+1}^{n} \mathbf{Y}_j^p(k)[\hat{\mathbf{X}}^p(k)]^{-1}. \tag{13}$$

With unequal weight coefficients, $\hat{\mathbf{H}}_j^{n+1}(k)$ can be expressed as follows:

$$\hat{\mathbf{H}}_j^{n+1}(k) = \sum_{p=n-L+1}^{n} \frac{\alpha^{n-p}(1-\alpha)}{1-\alpha^L}\mathbf{Y}_j^p(k)[\hat{\mathbf{X}}^p(k)]^{-1}. \tag{14}$$

Based on the encoding matrix of STBC, $\hat{\mathbf{X}}^n(k)$ is always invertible, ensuring the implementation of Equations (13) and (14).

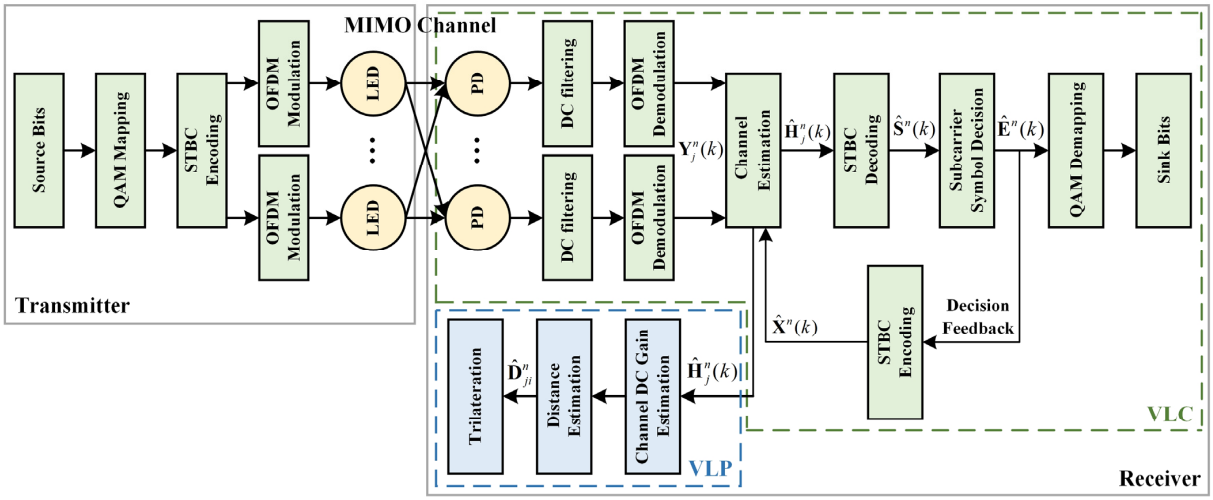

Figure 3. Block diagram of the integrated mobile VLCP scheme for MIMO configuration.

The acquired CSI can be further employed to determine the location of the mobile receiver. By setting $k = 1$ in the estimated FDTF $\hat{H}_{ji}^n(k)$ and referring to Equation (7), the distance between the ith LED and the jth PD can be estimated as follows:

$$\hat{D}_{ji}^n = \sqrt[m+3]{\frac{(m+1)AT_s(\varphi)g(\varphi)h^{m+1}}{2\pi\left|\hat{H}_{ji}^n(1)\right|}}. \tag{15}$$

With trilateration, we select different groups of the estimated distances to obtain multiple solutions for PD1, denoted as $(\hat{x}_{r1}^q, \hat{y}_{r1}^q)$ (q = 1, 2, 3, 4), and for PD2, denoted as $(\hat{x}_{r2}^q, \hat{y}_{r2}^q)$, similar to the MISO system. Then, the multiple solutions of the horizontal coordinate of the receiver are calculated as the midpoint between PD1 and PD2, i.e., $((\hat{x}_{r1}^q + \hat{x}_{r2}^q)/2, (\hat{y}_{r1}^q + \hat{y}_{r2}^q)/2)$. Taking the average among them can finally lead to the final positioning result.

3. Results and Discussion

In this section, we consider a 5 m × 5 m × 3 m indoor integrated mobile VLCP system model, depicted in Figure 1. The transmitter consists of four LEDs, while the mobile receiver moves at a constant velocity. As illustrated in Figure 4, we investigate several test routes for the mobile receiver: Route 1 from (1, 2.5, 0.85) to (4, 2.5, 0.85), Route 2 from (1, 3.5, 0.85) to (4, 3.5, 0.85), Route 3 from (1, 2.5, 0.85) to (2, 2.5, 0.85), and Route 4 from (1, 3.5, 0.85) to (2, 3.5, 0.85). Throughout these routes, we calculate the average BERs and positioning errors of the receiver. We explore both MISO and MIMO scenarios to analyze the system performance.

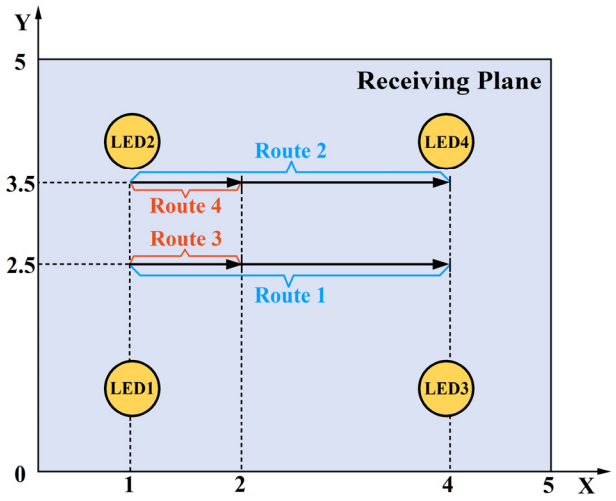

Figure 4. Bird's eye view of different test routes in the receiving plane.

In the MISO scenario, 4-QAM symbols are modulated into DCO-OFDM signals, which are then loaded onto four LEDs in the form of the LED selection matrix. All active LEDs transmit identical DCO-OFDM signals simultaneously, propagating through multipath channels. The mobile receiver, equipped with a single PD, utilizes DFCE to detect and recover the VLC signal. The CSI derived from the multipath channels is then employed for VLP. In the MIMO scenario, we consider a 4×2 MIMO system model, with a mobile receiver equipped with two PDs positioned 30 cm apart, maintaining a fixed pointing direction. 4-QAM symbols are generated, encoded with STBC, and then modulated into DCO-OFDM signals. These signals are transmitted through the mobile MIMO channel. At the receiver, the VLC signal is detected and recovered using DFCE with the dual-PD setup. Simultaneously, the CSI obtained from the VLC signal is utilized for VLP.

The OFDM symbol duration is standardized to 10 µs, with 512 subcarrier channels and a 20% cyclic prefix. For the MISO scenario, we assume that each OFDM packet consists of 2500 VLCP data blocks, with 35 blocks serving as training data. For the MIMO scenario, each OFDM packet also consists of 2500 VLCP data blocks, but with 20 blocks serving as training data. Consequently, the total duration of an OFDM packet is 0.1 s, and each OFDM packet conveys 10,000 OFDM symbols for MISO and 7500 OFDM symbols for MIMO. We then compare the communication and positioning performance of two schemes. The first scheme utilizes only OFDM training symbols at the start of each packet to estimate the CSI during terminal movement, without employing DFCE. In contrast, the second scheme integrates DFCE along with training symbols for enhanced CSI estimation. Except for Figure 12, equal weight coefficients are considered for DFCE. Additionally, the time interval for mobile VLP is set to 10 ms. For proof-of-concept, we only focus on line-of-sight (LOS) channels. When non-LOS channel conditions occur, the positioning accuracy can potentially be improved with machine learning [33], but this is beyond the scope of this paper. Other key parameters are provided in Table 1. The distribution of LEDs can affect the performance of the VLCP system. For the MISO scenario, if LEDs are positioned closely together and centrally in the ceiling, the multipath effect of the VLC channel becomes less obvious, making it difficult for the receiver to distinguish multipath components and accurately estimate the CSI for VLCP. For the MIMO scenario, closely placed LEDs in the center of the ceiling lead to a high correlation between channels, which can negatively affect the demodulation performance for VLCP. To ensure both effective communication and accurate positioning, while also maintaining uniform light distribution, we keep a certain distance between LEDs. Thus, we distribute the LEDs at the corners of the ceiling, with their coordinates listed in Table 1.

Table 1. Configuration parameters of mobile VLCP system.

Parameters	Values
Room size (length × width × height)	5 m × 5 m × 3 m
Transmit power per lamp (except for Figure 5)	25 Watt
Locations of LED1, LED2, LED3, and LED4	(1, 1, 3), (1, 4, 3), (4, 1, 3), (4, 4, 3)
Initial locations of PD1 and PD2 (for Routes 1 and 3)	(1.11, 2.61, 0.85), (0.89, 2.39, 0.85)
Initial locations of PD1 and PD2 (for Routes 2 and 4)	(1.11, 3.61, 0.85), (0.89, 3.39, 0.85)
Modulation index	0.25
Height of receiving plane	0.85 m
Physical area of PDs	10^{-4} m^2
Refractive index	1.5
PDs' field of view	85 deg.
Responsivity of PDs	0.35 A/W
Receiver velocity (except for Figures 6, 11, and 12)	1 m/s
Effective data rate for the MISO/MIMO scenario	51.2 Mbps/38.4 Mbps
Observation block length (except for Figure 10)	35 or 20

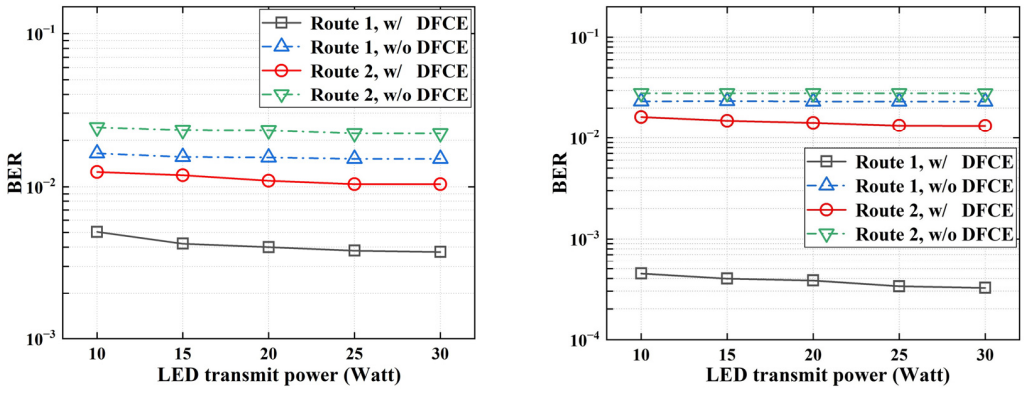

Figure 5. Comparison of system BER performance with and without DFCE under varying LED transmit power levels: (**a**) MISO scenario; (**b**) MIMO scenario.

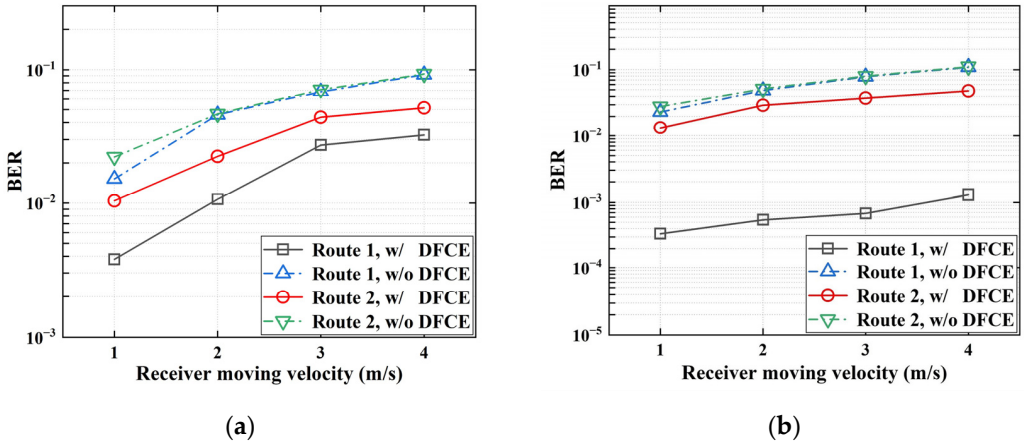

Figure 6. Comparison of system BER performance with and without DFCE at different receiver moving velocities: (**a**) MISO scenario; (**b**) MIMO scenario.

We first evaluate the communication performance of the mobile VLCP systems. Figure 5 compares the BERs for the MISO and MIMO systems under different LED transmit powers. In Figure 5a, we observe a significant improvement in BER with the implementation of DFCE in the mobile MISO system. For instance, at a transmit power of 25 W, the BERs without DFCE are 1.5×10^{-2} and 2.2×10^{-2} for receiver movement along Route 1 and Route 2, respectively. After using DFCE, the BERs improve to 3.8×10^{-3} and 1.0×10^{-2} for Route 1 and Route 2, respectively. This enhancement is attributed to the increased channel estimation accuracy of DFCE, enabling effective tracking of the time-varying channel and improved signal recovery. Additionally, we observe a slight reduction in BER as the transmit power increases, although the effect is not significant. However, the influence of different routes on BER is more evident. Route 1 exhibits notably better performance than Route 2, primarily due to its closer proximity to the room center, resulting in higher SNRs. In Figure 5b, the MIMO system exhibits similar trends to the MISO system in Figure 5a. For example, in Route 1 at a transmit power of 25 W, the BER improves from 2.3×10^{-2} to 3.3×10^{-4} with the adoption of DFCE. Thus, DFCE demonstrates its capability to enhance the communication quality of the mobile MIMO system as well.

Figure 6 compares the BER performance of the MISO and MIMO systems at varying receiver moving velocities. As illustrated in Figure 6a, increased velocity leads to BER degradation across all schemes for MISO. For instance, with the velocity increasing from 1 m/s to 4 m/s, the BER without DFCE rises from 1.5×10^{-2} to 9.2×10^{-2} and from 2.2×10^{-2} to 9.3×10^{-2} for receiver movement along Route 1 and Route 2, respectively. This deterioration is a result of higher velocities inducing quicker channel variations, which negatively impact channel estimation accuracy, particularly in scenarios without feedback. However, after using DFCE, the BER of the MISO system is improved. For example, at velocities of 1 m/s and 4 m/s in Route 1, the BER improves to 3.8×10^{-3} and 3.2×10^{-2}, respectively. In Figure 6b, similar trends are observed for the MIMO scenario. For instance, in Route 1, the BER with DFCE improves from 4.9×10^{-2} to 5.4×10^{-4} and from 1.1×10^{-1} to 1.3×10^{-3} at velocities of 2 m/s and 4 m/s, respectively. In Route 2, at 1 m/s, the BER with DFCE improves from 2.8×10^{-2} to 1.3×10^{-2}. These results highlight the effectiveness of DFCE in accurately estimating the time-varying channel and recovering the transmitted signal, especially at higher velocities.

Next, we assess the positioning performance of the mobile VLCP systems. Figure 7 displays the positioning results for the MISO and MIMO systems when the receiver moves along different routes. In both scenarios and routes, when DFCE is not utilized, the positioning results are only obtained at discrete locations near the receiver's moving trajectories. This limitation arises from solely using training symbols for channel estimation, resulting in a constant CSI estimation throughout the entire OFDM packet. Consequently, the positioning results in each packet overlap at the same locations. After employing DFCE, continuous positioning results become apparent, being in much closer alignment with the actual locations. This improvement is attributed to the ability of DFCE to dynamically estimate the channel, thereby yielding more accurate CSI. This accurate CSI, in turn, contributes to enhanced positioning accuracy within the VLCP system. Furthermore, in Figure 7b, due to the receiver's higher SNRs in Route 1, the positioning accuracy appears to be superior compared to Route 2 for the MIMO system. Therefore, the VLCP scheme with DFCE can leverage the advantages of higher SNRs to enhance positioning accuracy.

In Figure 8, we compare the cumulative distribution functions (CDFs) of positioning errors calculated from the results in Figure 7, for both the MISO and MIMO systems. For the MISO system in Figure 8a, before using DFCE, 90% of positioning errors are less than 9.5 cm and 9.4 cm when the receiver moves along Route 1 and Route 2, respectively. After using DFCE, these errors decrease to 5.8 cm and 7.5 cm, respectively. Similar trends are observed in the MIMO system in Figure 8b. Along Route 1, before employing DFCE, 90% of positioning errors are less than 8.2 cm. However, this error reduces to 4.0 cm with the adoption of DFCE. The advantage of DFCE becomes more obvious along Route 2. Without DFCE, 90% of positioning errors are less than 22.4 cm. However, this error significantly

reduces to 16.5 cm when DFCE is employed. These findings validate the effectiveness of the feedback mechanism in enhancing mobile positioning accuracy.

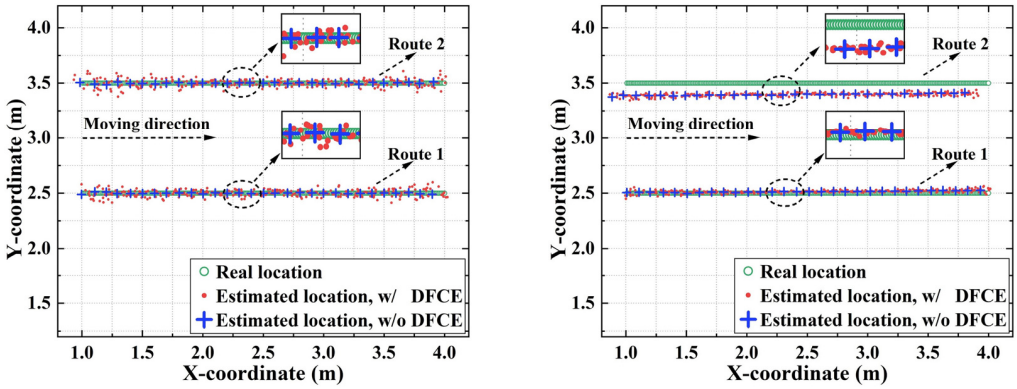

Figure 7. Results for mobile VLP with and without DFCE as the receiver moves along different test routes: (**a**) MISO scenario; (**b**) MIMO scenario.

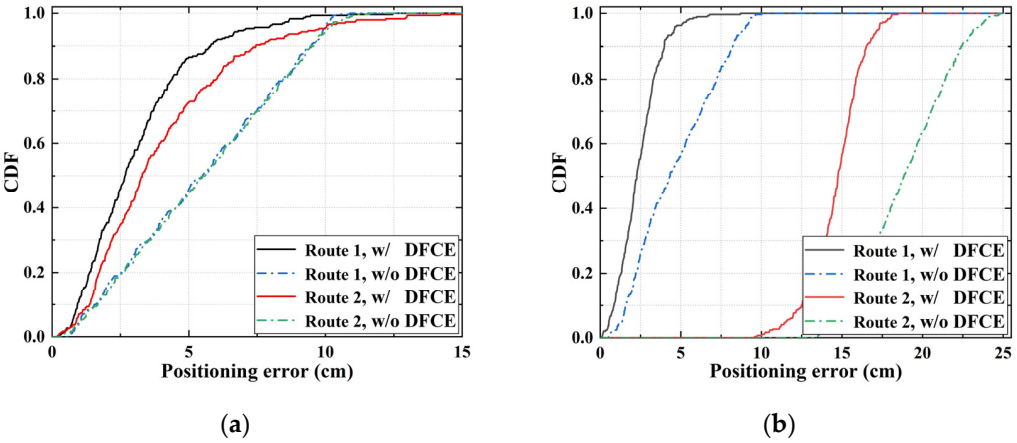

Figure 8. Comparison of CDFs for positioning errors with and without DFCE: (**a**) MISO scenario; (**b**) MIMO scenario.

It is worth mentioning that the BERs and positioning errors mentioned above are average values observed while the receiver moves along different routes. For VLC, the BERs are linked to the performance of all subcarrier channels. When channel characteristics degrade, error propagation due to decision feedback, which is a weakness of DFCE, impacts overall BER performance. This issue is particularly pronounced when light intensity is low. However, the CSI used for positioning remains accurate as it only depends on the estimated FDTF of the first subcarrier channel, as shown in Equations (6) and (15). At $k = 1$, subcarrier symbols experience a higher channel response and greater noise robustness compared to others. Therefore, even at overall BER levels higher than 10^{-3} as in Figures 5 and 6, positioning errors are still maintained at the centimeter level. To further explain this, Figure 9 compares the eye diagrams of the real part for the received 4-QAM symbols in different subcarrier channels equalized with DFCE in Route 2. In both MISO and MIMO scenarios, we can clearly see that for $k = 1$, due to higher noise robustness, the eye diagram is clear and open. Conversely, for $k = 100$, due to lower noise robustness and the high possibility of error propagation from decision feedback, the eye diagram is closed, indicating poor performance. To address this issue, a possible solution is to use machine learning to mitigate the error propagation of DFCE and improve the channel equalization performance [34].

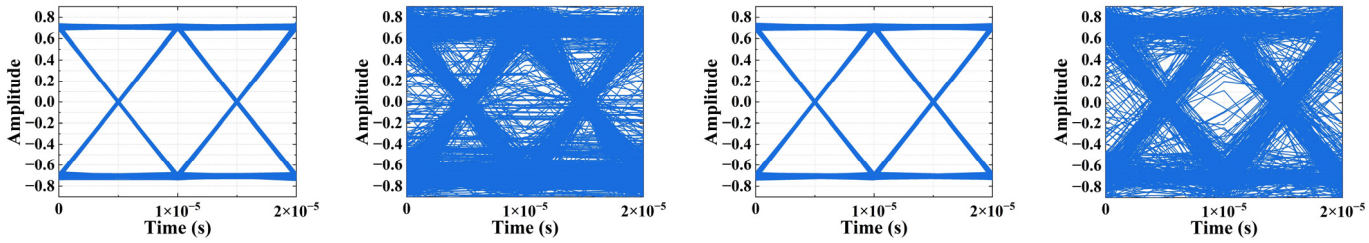

(**a**) (**b**) (**c**) (**d**)

Figure 9. Eye diagrams of the real part for the received 4-QAM symbols equalized with DFCE in Route 2: (**a**) MISO scenario, k = 1; (**b**) MISO scenario, k = 100; (**c**) MIMO scenario, k = 1; (**d**) MIMO scenario, k = 100.

Next, we examine the impact of observation block length L on positioning performance. Figure 10 compares the mean positioning errors obtained in the VLCP system using different L values for the MISO and MIMO systems. In both scenarios, we generally observe improved positioning accuracy with increasing L. For instance, for the MISO system in Figure 10a, along Route 1, the mean positioning error with DFCE decreases from 3.4 cm to 3.1 cm when L is increased from 25 to 35. This improvement is attributed to the longer observation block length effectively equalizing the channel and averaging out noise, resulting in more accurate CSI for mobile VLP. However, further increasing L does not lead to significant enhancement in positioning accuracy, particularly when L exceeds 40 for the MISO system. Similarly, for the MIMO system in Figure 10b, there is no significant enhancement when L exceeds 20. Because longer observation block lengths result in higher computing and storage requirements at the receiver, to balance system complexity and positioning accuracy, an optimal L value could be selected around 35 and 20 for MISO and MIMO systems, respectively, when DFCE is employed. This selection yields mean positioning errors of 3.1 cm for the MISO system and 2.4 cm for the MIMO system in Route 1.

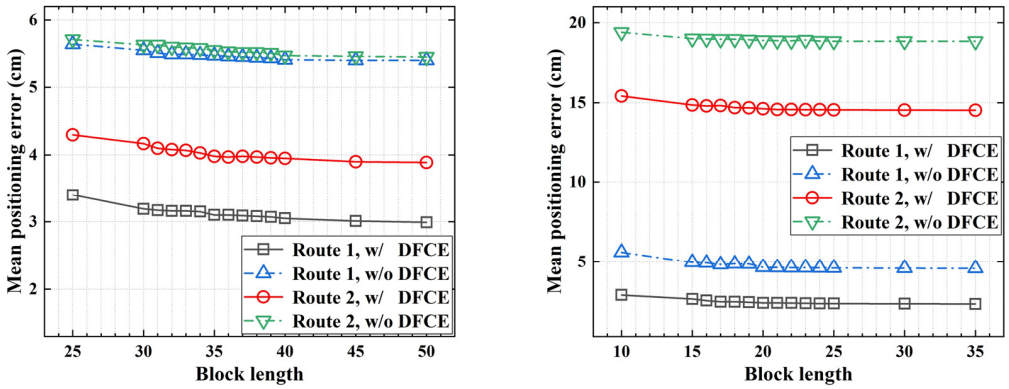

(**a**) (**b**)

Figure 10. Comparison of mean positioning errors with and without DFCE for different observation block lengths: (**a**) MISO scenario; (**b**) MIMO scenario.

Figure 11 compares the positioning performance for the MISO and MIMO scenarios at different receiver moving velocities. For the MISO system in Figure 11a, we observe a significant increase in mean positioning errors with increasing velocity when DFCE is not employed. For instance, in Route 1, the mean positioning error increases from 5.5 cm to 21.3 cm when the velocity increases from 1 m/s to 4 m/s. Similarly, in Route 2, the mean positioning error increases from 5.6 cm to 21.5 cm with the same change in velocity. This is due to the faster channel variations caused by higher velocities, which result in reduced

channel estimation accuracy. However, when DFCE is employed to track and estimate the time-varying channel, the positioning errors remain relatively stable, ranging from 3.1 cm to 3.6 cm in Route 1 and from 4.0 cm to 4.3 cm in Route 2. In the MIMO system, the results exhibit a similar trend to the MISO system, with errors ranging from 2.4 cm to 2.5 cm in Route 1 and from 14.6 cm to 14.9 cm in Route 2. This indicates the effectiveness of DFCE in maintaining stable positioning performance regardless of the terminal moving speed.

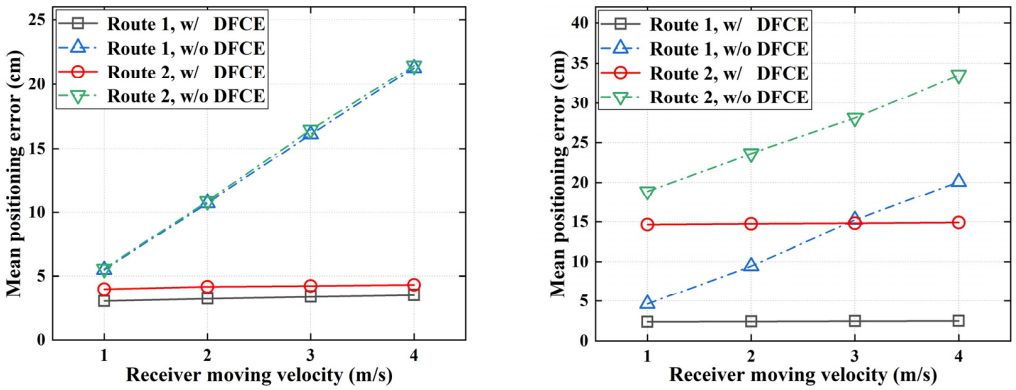

Figure 11. Comparison of mean positioning errors with and without DFCE at different receiver velocities: (**a**) MISO scenario; (**b**) MIMO scenario.

Next, we assess the impact of different weight coefficients on the positioning performance with DFCE. Considering various values of the forgotten factor α in Equations (9) and (14), Figure 12 compares the mean positioning errors under different weight coefficients for the MISO and MIMO systems. Here, the terminal velocity is set at 4 m/s. For the MISO system in Figure 12a, with equal weight coefficients, an increase in the number of subcarriers leads to higher mean positioning errors. For example, as the number of subcarriers increases from 128 to 1024, the mean positioning error increases by 1.2 cm and 1.8 cm when the receiver moves along Route 3 and Route 4, respectively. This occurs because, under a constant data rate, more subcarriers result in longer OFDM symbol durations, extending the decision feedback duration and causing more significant channel variations. However, more appropriate weight coefficients can improve positioning performance. For instance, in Route 4, when the number of subcarriers is 1024, the mean positioning error is optimized with α = 0.7, resulting in 4.8 cm, compared to 6.0 cm with equal weight coefficients. Increasing the weight for estimated CSI in VLCP data blocks adjacent to the current channel can enhance the accuracy of channel estimation due to their high correlation. However, higher weights also amplify the impact of noise, underscoring the importance of selecting appropriate weights. Similarly, in the MIMO system, optimal weight coefficients occur when α = 0.7 in both Route 3 and Route 4.

Finally, considering the variation in terminal size in our MIMO-based VLCP system, we assess the positioning performance by adjusting the distance between the two PDs. Figure 13 compares the mean positioning errors with and without DFCE at different PD distances. Along Route 1, where the SNR is sufficient, increasing the distance between PDs does not notably enhance the positioning performance. However, in Route 2, without DFCE, the mean positioning error can be reduced from 20.0 cm to 17.5 cm as the distance between PDs increases from 20 cm to 50 cm. After employing DFCE, the mean positioning error can be further reduced from 15.5 cm to 12.5 cm. This improvement is attributed to the decreased correlation between channels as the distance between PDs increases, resulting in reduced interference between signals and less additional noise being introduced.

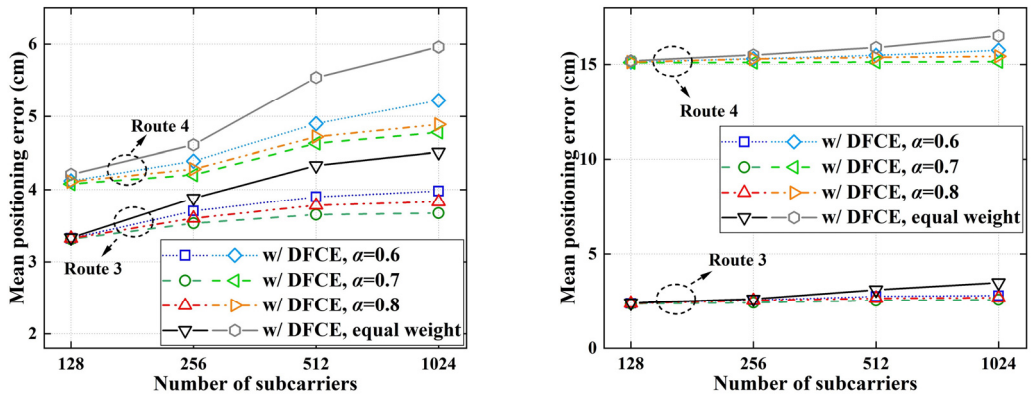

Figure 12. Comparison of mean positioning errors with DFCE when using different weight coefficients: (**a**) MISO scenario; (**b**) MIMO scenario.

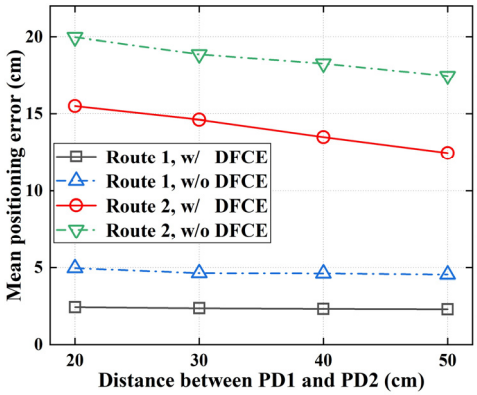

Figure 13. Comparison of mean positioning errors in MIMO with different PD distances.

4. Conclusions

We proposed an integrated mobile VLCP scheme capable of simultaneously integrating VLC and VLP into a single system. By employing DFCE for accurate estimation of time-varying CSI, we enhanced the performance of both communication and positioning under mobile receiver scenarios. Our approach considers VLCP for both MISO and MIMO scenarios, utilizing multipath channels for CSI extraction in MISO and employing STBC for CSI estimation in MIMO. Comprehensive simulations were conducted to evaluate performance. The results showed that in the MISO system, when utilizing DFCE, the BER is 3.8×10^{-3} and 1.0×10^{-2}, with 90% of positioning errors less than 5.8 cm and 7.5 cm when the receiver moves along Route 1 and Route 2, respectively. In the MIMO system, with DFCE employed, the BER is 3.3×10^{-4} and 1.3×10^{-2}, with 90% of positioning errors less than 4.0 cm and 16.5 cm in Route 1 and Route 2, respectively. Furthermore, optimizing weight coefficients and increasing PD distance for MIMO receivers can effectively enhance positioning accuracy. In future work, we will consider 3D positioning and receiver tilt.

Author Contributions: Conceptualization, X.Y.; methodology, R.W., Y.S. and X.Y.; software, R.W., Y.S. and Z.L.; validation, R.W. and Y.S.; formal analysis, R.W. and Y.S.; investigation, R.W. and Z.L.; resources, M.G. and X.Y.; data curation, R.W.; writing—original draft preparation, R.W. and X.Y.; writing—review and editing, M.G. and X.Y.; visualization, R.W. and Z.L.; supervision, X.Y.; project administration, X.Y.; funding acquisition, X.Y. All authors have read and agreed to the published version of the manuscript.

Funding: This research was funded by the National Natural Science Foundation of China (62001319), Suzhou Science and Technology Bureau-Technical Innovation Project in Key Industrial (SYG202112), and Open Fund of IPOC (BUPT) (IPOC2020A009).

Institutional Review Board Statement: Not applicable.

Informed Consent Statement: Not applicable.

Data Availability Statement: The raw data supporting the conclusions of this article will be made available by the authors on request.

Conflicts of Interest: The authors declare no conflicts of interest.

References

1. Liu, X.; Guo, L.; Wei, X. Indoor visible light applications for communication, positioning, and security. *Wirel. Commun. Mob. Com.* **2021**, *2021*, 1730655. [CrossRef]
2. Karunatilaka, D.; Zafar, F.; Kalavally, V.; Parthiban, R. LED based indoor visible light communications: State of the art. *IEEE Commun. Surv. Tutor.* **2015**, *17*, 1649–1678. [CrossRef]
3. Zvanovec, S.; Chvojka, P.; Haigh, P.A.; Ghassemlooy, Z. Visible light communications towards 5G. *Radioengineering* **2015**, *24*, 1–9. [CrossRef]
4. Zhuang, Y.; Hua, L.; Qi, L.; Yang, J.; Cao, P.; Cao, Y.; Wu, Y.; Thompson, J.; Haas, H. A survey of positioning systems using visible LED lights. *IEEE Commun. Surv. Tutor.* **2018**, *20*, 1963–1988. [CrossRef]
5. Pang, M.; Shen, G.; Yang, X. Achieving reliable underground positioning with visible light. *IEEE Trans. Instru. Meas.* **2022**, *71*, 1–15. [CrossRef]
6. Maheepala, M.; Kouzani, A.Z.; Joordens, M.A. Light-based indoor positioning systems: A review. *IEEE Sens. J.* **2020**, *20*, 3971–3995. [CrossRef]
7. Lin, X.; Zhang, L. Intelligent and practical deep learning aided positioning design for visible light communication receivers. *IEEE Commun. Lett.* **2020**, *24*, 577–580. [CrossRef]
8. Chen, J.; You, X. Visible light positioning and communication cooperative systems. In Proceedings of the 2017 16th International Conference on Optical Communications and Networks (ICOCN), Wuzhen, China, 7–10 August 2017; pp. 1–3. [CrossRef]
9. Yang, H.; Chen, C.; Zhong, W.; Alphones, A.; Zhang, S.; Du, P. Demonstration of a quasi-gapless integrated visible light communication and positioning system. *IEEE Photon. Technol. Lett.* **2018**, *30*, 2001–2004. [CrossRef]
10. Yang, H.; Zhong, W.; Chen, C.; Alphones, A.; Du, P. QoS-driven optimized design-based integrated visible light communication and positioning for indoor IoT networks. *IEEE Internet Things J.* **2020**, *7*, 269–283. [CrossRef]
11. Xu, Y.; Wang, Z.; Liu, P.; Chen, J.; Han, S.; Yu, C.; Yu, J. Accuracy analysis and improvement of visible light positioning based on VLC system using orthogonal frequency division multiple access. *Opt. Express.* **2017**, *25*, 32618–32630. [CrossRef]
12. Yang, H.; Zhong, W.; Chen, C.; Alphones, A.; Du, P.; Zhang, S.; Xie, X. Coordinated resource allocation-based integrated visible light communication and positioning systems for indoor IoT. *IEEE Trans. Wirel. Commun.* **2020**, *19*, 4671–4684. [CrossRef]
13. Ma, S.; Yang, R.; Du, C.; Li, H.; Wu, Y.; Al-Dhahir, N.; Li, S. Robust power allocation for integrated visible light positioning and communication networks. *IEEE Trans. Commun.* **2023**, *71*, 4764–4777. [CrossRef]
14. Chen, D.; Fan, K.; Wang, J.; Lu, H.; Jin, J.; Feng, L.; Chen, H.; Xue, Z.; Wang, Y. Integrated visible light communication and positioning CDMA system employing modified ZCZ and Walsh code. *Opt. Express* **2022**, *30*, 40455–40469. [CrossRef] [PubMed]
15. Liu, Z.; Yu, C. Multi-user visible light communication and positioning system based on dual-domain multiplexing scheme. *Photonics* **2023**, *10*, 306. [CrossRef]
16. Liu, Z.; You, X.; Chen, J.; Yu, C. Two-LED indoor visible light positioning method based on channel estimation with a mirror. In Proceedings of the 2019 Asia Communications and Photonics Conference (ACP), Chengdu, China, 2–5 November 2019; pp. 1–2. Available online: https://ieeexplore.ieee.org/document/8989700 (accessed on 10 February 2020).
17. Wang, K.; Liu, Y.; Hong, Z. RSS-based visible light positioning based on channel state information. *Opt. Express* **2022**, *30*, 5683–5699. [CrossRef]
18. Deng, L.; Fan, Y.; Zhao, Q.; Wu, P. Indoor visible light positioning based on channel estimation and cramér–rao low bound analysis with random receiving orientation of user equipment. *Photonics* **2023**, *10*, 812. [CrossRef]
19. Hong, Y.; Chen, L.K. Toward user mobility for OFDM-based visible light communications. *Opt. Lett.* **2016**, *41*, 3763–3766. [CrossRef] [PubMed]
20. You, X.; Zhong, Y.; Chen, J.; Yu, C. Mobile channel estimation based on decision feedback in vehicle-to-infrastructure visible light communication systems. *Opt. Commun.* **2020**, *462*, 125261. [CrossRef]
21. Shao, Y.; Hong, Y.; Deng, R.; Chen, L.K. Performance enhancement by spatial diversity for robust VLC systems with fast-moving terminals. In Proceedings of the 2019 Optoelectronics and Communications Conference (OECC) and 2019 International Conference on Photonics in Switching and Computing (PSC), Fukuoka, Japan, 7–11 July 2019; pp. 1–3. [CrossRef]
22. Li, C.; Yi, Y.; Lee, K.; Lee, K. Performance analysis of visible light communication using the STBC-OFDM technique for intelligent transportation systems. *Int. J. Electron.* **2013**, *101*, 1117–1133. [CrossRef]

23. Souto, V.D.P.; Dester, P.S.; Facina, M.S.P.; Silva, D.G.; de Figueiredo, F.A.P.; Tejerina, G.R.D.; Santos, J.C.S.; Ferreira, J.S.; Mendes, L.L.; Souza, R.D.; et al. Emerging MIMO technologies for 6G networks. *Sensors* **2023**, *23*, 1921. [CrossRef]
24. Khwandah, S.A.; Cosmas, J.P.; Lazaridis, P.I.; Zaharis, Z.D.; Chochliouros, I.P. Massive MIMO systems for 5G communications. *Wirel. Pers. Commun.* **2021**, *120*, 2101–2115. [CrossRef]
25. Zheng, H.; Xu, Z.; Yu, C.; Gurusamy, M. A 3-D high accuracy positioning system based on visible light communication with novel positioning algorithm. *Opt. Commun.* **2017**, *396*, 160–168. [CrossRef]
26. Huang, N.; Gong, C.; Luo, J.; Xu, Z. Design and demonstration of robust visible light positioning based on received signal strength. *J. Light. Technol.* **2020**, *38*, 5695–5707. [CrossRef]
27. Tran, H.Q.; Ha, C. Improved visible light-based indoor positioning system using machine learning classification and regression. *Appl. Sci.* **2019**, *9*, 1048. [CrossRef]
28. Wei, T.; Liu, S.; Du, X. Visible light integrated positioning and communication: A multi-task federated learning framework. *IEEE Trans. Mobile Comput.* **2023**, *22*, 7086–7103. [CrossRef]
29. Wei, Y.; Liu, X.; Wang, Y.; Ma, S.; Zhou, F.; Dobre, O.A. Channel and location estimation enabled a novel BDCNP network for massive MIMO VLCP systems. *IEEE Wirel. Commun. Lett.* **2024**, *13*, 218–222. [CrossRef]
30. Sun, Y.; You, X.; Chen, J.; Yu, M.; Gao, M.; Shen, G. Decision feedback channel estimation for integrated mobile VLCP based on STBC-MIMO. In Proceedings of the 2023 Asia Communications and Photonics Conference/2023 International Photonics and Optoelectronics Meetings (ACP/POEM), Wuhan, China, 4–7 November 2023; pp. 1–4. [CrossRef]
31. Gfeller, F.R.; Bapst, U. Wireless in-house data communication via diffuse infrared radiation. *Proc. IEEE* **1979**, *67*, 1474–1486. [CrossRef]
32. Damen, M.O.; Gamal, H.E.; Beaulieu, N.C. Linear threaded algebraic space-time constellations. *IEEE Trans. Inf. Theory* **2003**, *49*, 2372–2388. [CrossRef]
33. Abou-Shehada, I.M.; AlMuallim, A.F.; AlFaqeh, A.K.; Muqaibel, A.H.; Park, K.H.; Alouini, M.S. Accurate indoor visible light positioning using a modified pathloss model with sparse fingerprints. *J. Light. Technol.* **2021**, *39*, 6487–6497. [CrossRef]
34. Xu, J.; Li, L.; Zheng, L.; Liu, L. Detect to learn: Structure learning with attention and decision feedback for MIMO-OFDM receive processing. *IEEE Trans. Commun.* **2024**, *72*, 146–161. [CrossRef]